

Extremely Correlated Fermi Liquids: Self consistent solution of the second order theory

Daniel Hansen and B. Sriram Shastry

Physics Department, University of California, Santa Cruz, CA 95064, USA

(Dated: November 1, 2012)

We present detailed results from a recent microscopic theory of extreme correlated Fermi liquids, applied to the t - J model in two dimensions. We use two typical sets of band parameters relevant to the cuprate superconductors. The second order theory in the parameter λ is valid in the overdoped regime where $0 \leq n \lesssim 0.7$, where n is the particle density (related to hole density x by $n = 1 - x$). The calculation involves the self consistent solution of equations for an auxiliary Fermi liquid type Greens function and an adaptive spectral weight, or caparison factor, described in recent papers by Shastry (Ref. (1), Ref. (5)). We present the numerical results at low as well as high T at various low densities in the normal phase. We display the (two) chemical potential(s), the momentum space occupation function m_k , various energy dispersions locating the peaks of spectral functions, the optical conductivity, relaxation rates for quasiparticles, and the electronic spectral functions along various directions and with typical additional elastic scattering. The line shapes have characteristic shapes that are very similar to those from approximate treatments of the equations in recent work, and display frequently observed features such as the high energy kink, that depend on the bare band dispersion.

Contents

I. Introduction	1
II. Summary of the $O(\lambda^2)$ Theory	2
III. Computation of Spectral Functions	3
A. Definitions	3
B. Flowchart of the Iterative process	4
C. Fast Fourier Transforms for evaluating convolutions	5
IV. Results	6
A. Physical Variables	6
B. Other parameters in the programs	6
C. Thermodynamics	7
D. Frequency independent Variables	7
E. Quasiparticle Dispersion and Z_k	9
F. Self energies	12
G. Spectral Functions and ARPES Lineshapes	13
H. Optical conductivity	16
V. Concluding remarks	16
VI. Acknowledgements	19
References	19

I. INTRODUCTION

The t - J model describes the problem of extremely strongly interacting spin half Fermi systems, made difficult by the requirement of at most single occupancy of the lattice sites. It is the subject of many recent works in the context of the Cuprate superconductors and other correlated systems. This is also a very hard problem since standard methods such as perturbative expansions fail, thereby motivating a new strong coupling approach to the resulting in the theory of *extremely correlated Fermi liquids* Ref. (1), denoted by ECFL. Previous applications to the two dimensional cuprate systems of the ideas in Ref. (1) have been approximate, but have given encouraging results. The spectral functions of

electrons that compare very well with the experimental Angle Resolved Photo Emission (ARPES) data as in Ref. (2), and lead to interesting predictions for the asymmetry of line shapes as in Ref. (3), as well as to unusual forms of electronic propagators in these systems Ref. (4).

The recent work Ref. (5) provides a detailed set of equations following from the above ECFL theory, which are the main focus of this work. We will refer to this theory as (I) here and prefix equations of that paper with (I). The equations are to second order in the parameter λ of that theory, related to the density of double occupation. Broadly speaking, these equations generalize the fully self consistent skeleton diagram expansion of the canonical Fermi liquid theory, as described in texts Ref. (6), Ref. (7), Ref. (8) to the case of extreme correlations, and take care to satisfy the important *shift invariance*⁵ of the t - J model to each order. In this paper, we present the first detailed calculations from ECFL by solving the above equations to evaluate some thermodynamical variables, the spectral functions, ARPES line shapes and optical conductivity of the t - J model. Our calculations are valid in the high hole doping limit, i.e. the overdoped regime which is also the region of low *electron density*, so that the second order theory in λ is valid. Future work will be aimed at higher order calculations in λ which would enable us to address densities close to optimal doping. The results compared with other approximations as well as a few experiments.

While analytical methods beyond crude mean field theories have been in short supply, there is a valuable body of numerical results for the t - J model from exact diagonalization Ref. (9), high temperature series expansions¹⁰, finite temperature Lanczos methods^{11–14}, and variational wave functions^{15–17}. Noteworthy are the results of Ref. (12) from Prelovsek and co workers, who handle the series expansion in inverse temperature in a stochastic fashion, thereby obtaining results down to fairly low temperatures. Owing to finite size effects and the inherent nature of the high T expansion, the results from this theory, although broadly comparable to ours, seem more grainy. The Hubbard model at large U tends to the t - J model so the large U studies of this model are of interest. Quantum Monte Carlo methods, despite the difficulties associated with the sign problem, yield some valuable insights into the spectral features such as kinks¹⁸. The dynamical mean field theory for the Hubbard model^{19,20} gives a numerically exact solution in high enough dimensions of the model, and although strong coupling, i.e. $U > W$ is challenging, there is impressive progress overall. The recent paper Ref. (21) at strong coupling i.e. large U/t obtains detailed spectral functions that are roughly comparable to what we find here for the t - J model.

The work proceeds as follows. In Section (II) we present a summary of the equations solved here from Ref. (5). In Section (III) we discuss the computational strategy and explain the scheme, using the Fast Fourier Transform method (FFT), so that the spectral functions can be computed efficiently. Section (IV) presents the detailed results of the calculation. Section (V) contains a summary and some concluding comments.

II. SUMMARY OF THE $O(\lambda^2)$ THEORY

In this theory the physical Greens function \mathcal{G} is obtained from:

$$\mathcal{G}(k) = \mathbf{g}(k) \mu(k) = \frac{\mu(k)}{i\omega_n + \boldsymbol{\mu} - \bar{\varepsilon}_k - \bar{\Phi}(k)}. \quad (1)$$

Here $\mu(k)$, termed the caparison factor, plays the role of an adaptive spectral weight while $\mathbf{g}(k)$ is a canonical Fermi liquid, derivable from a Luttinger Ward functional. In general both $\mu(k)$ and $\mathbf{g}^{-1}(k)$ can be expanded to a given order in the parameter λ . Consequently we have two "self energies" denoted by $\bar{\Phi}$ and Ψ , which determine $\mathbf{g}(k)$ and $\mu(k)$. The second order equations studied in detail in this work, are described by equations (I-83, I-84, I-85) for the Greens functions:

$$\mu(k) = 1 - \lambda \frac{n}{2} + \lambda^2 \frac{n^2}{4} + \lambda^2 \Psi(k), \quad \text{where } (k) \equiv (\vec{k}, i\omega_k), \quad (2)$$

$$\Psi(k) = - \sum_{p,q} (\varepsilon_p + \varepsilon_{k+q-p} + \varepsilon_k + \varepsilon_q + J_{k-p} - u_0) \mathbf{g}(p) \mathbf{g}(q) \mathbf{g}(q+k-p) \quad (3)$$

$$\mathbf{g}^{-1}(k) = i\omega_n + \boldsymbol{\mu} - \bar{\varepsilon}_k - \lambda^2 \bar{\Phi}(k) \quad (4)$$

$$\bar{\varepsilon}_k = \left(1 - \lambda n + \lambda^2 \frac{3n^2}{8}\right) \varepsilon_k + \lambda \sum_q \frac{1}{2} J_{k-q} \mathbf{g}(q) \quad (5)$$

$$\begin{aligned} \bar{\Phi}(k) = & - \sum_{q,p} \mathbf{g}(q) \mathbf{g}(p) \mathbf{g}(k+q-p) \\ & \times (\varepsilon_k + \varepsilon_p + \varepsilon_q + \varepsilon_{k+q-p} + J_{k-p} - u_0) \{ \varepsilon_k + \varepsilon_p + \varepsilon_q + \varepsilon_{k+q-p} + \frac{1}{2} (J_{k-p} + J_{p-q}) - u_0 \}. \end{aligned} \quad (6)$$

This is written with slight change of notation $[\Phi(k)]_1 \rightarrow \bar{\Phi}(k)$ from (I-85), and we have introduced the effective band energy $\bar{\varepsilon}_k$ in Eq. (5) that gets a static contribution from shrinking of the bare energies ε_k as well as from the exchange energy J . All terms are understood to be correct upto $O(\lambda^2)$, and possess corrections of $O(\lambda^3)$ that are ignored here. We set the parameter $\lambda \rightarrow 1$ in the following.

The number of the physical electrons is fixed by the first sum rule:

$$\frac{n}{2} = \sum_k \mathcal{G}(k) e^{i\omega_n 0^+}, \quad (7)$$

while the auxiliary Fermions described by \mathbf{g} are equal in number, and satisfy the sum rule:

$$\frac{n}{2} = \sum_k \mathbf{g}(k) e^{i\omega_n 0^+} \quad (8)$$

where $\sum_k \equiv \frac{1}{\beta} \sum_{\vec{k}, \omega_n}$. We thus determine the two independent chemical potentials μ and u_0 , so as to satisfy the two equations (Eq. (7) and Eq. (8)) simultaneously. Before discussing the computation we note that dropping terms of $O(\lambda^3)$ in Eq. (2) - Eq. (6) limits the regime of validity of these calculation to densities not too close to unity. From Eq. (2) we see that this theory would give a high frequency behavior of $\mathcal{G} \sim \frac{c_0}{i\omega}$ with $c_0 = 1 - \frac{n}{2} + \frac{n^2}{4}$, rather than the exact value $c_0 = 1 - \frac{n}{2}$. This slight error in the high frequency physics is a result of the expansion in λ , however the low frequency physics epitomized by the Luttinger Ward sum rule is exactly obeyed to each order in λ . Thus we have an error of $\sim 25\%$ in the high frequency spectral weight in this theory at $n \sim .78$, somewhat beyond where we can push this approximation. The $O(\lambda^3)$ terms would extend the range of this approximation to higher particle densities. In the following, we will study the Greens functions and the optical conductivity as well as some thermodynamic variables for the 2-d square lattice t - J model. The detailed parameters are listed below in Subsection IV A.

III. COMPUTATION OF SPECTRAL FUNCTIONS

A. Definitions

Computationally it is expedient to employ a spectral function notation as described for example in Ref. (8). The Matsubara frequency object $\mathcal{G}(k, i\omega_n)$ is analytically continued to the real axis and its spectral density written as:

$$\rho_{\mathcal{G}}(k, \nu) = -\frac{1}{\pi} \text{Im} [\mathcal{G}(k, i\omega \rightarrow \nu + i\eta)] \equiv A(k, \nu). \quad (9)$$

Here $A(k, \nu)$ is the same notation used in most experimental literature. The real part of the analytically continued function can be obtained by Hilbert transform

$$\text{Re } \mathcal{G}(k, \nu) = \text{P.V.} \int_{-\infty}^{\infty} \frac{\rho_{\mathcal{G}}(k, y)}{\nu - y} dy. \quad (10)$$

An analogous definition is given for spectral representation $\rho_{\mathbf{g}}(k, \nu)$, $\rho_{\bar{\Phi}}(k, \nu)$, $\rho_{\Psi}(k, \nu)$ used for \mathbf{g} , $\bar{\Phi}$, Ψ , etc, and hence the full set of equations above can be rewritten in terms of these spectral functions. Since \mathcal{G} is a product as in Eq. (1) we note that within the $O(\lambda^2)$ theory:

$$\rho_{\mathcal{G}}(k, \omega) = \rho_{\mathbf{g}}(k, \omega) \left(1 - \frac{n}{2} + \frac{n^2}{4} + \text{Re } \Psi(k, \omega) \right) + \rho_{\Psi}(k, \omega) \text{Re } \mathbf{g}(k, \omega), \quad (11)$$

so the two sumrules Eq. (8) and Eq. (7) can be written as:

$$\begin{aligned} \frac{n}{2} &= \sum_k \int d\omega \rho_{\mathbf{g}}(k, \omega) f(\omega) \\ \frac{n^2}{4} (1 - \frac{n}{2}) &= - \sum_k \int d\omega \left(\rho_{\mathbf{g}}(k, \omega) \text{Re } \Psi(k, \omega) + \text{Re } \mathbf{g}(k, \omega) \rho_{\Psi}(k, \omega) \right) f(\omega) \end{aligned} \quad (12)$$

where $f(\omega) = (1 + \exp(\beta\omega))^{-1}$ and $\bar{f}(\omega) = 1 - f(\omega)$. The auxiliary spectral function is the usual Dysonian form

$$\rho_{\mathbf{g}}(k, \omega) = \frac{\rho_{\bar{\Phi}}(k, \omega)}{\{\omega + \mu - \bar{\varepsilon}_k - \text{Re } \bar{\Phi}(k, \omega)\}^2 + (\pi \rho_{\bar{\Phi}})^2}. \quad (13)$$

The spectral functions for Ψ and $\bar{\Phi}$ have the form

$$\begin{aligned} \rho_{\bar{\Phi}}(k, \omega) = & \frac{1}{N_s^2} \sum_{pq} \int d\nu_1 d\nu_2 \rho_{\mathbf{g}}(p, \nu_1) \rho_{\mathbf{g}}(q, \nu_2) \rho_{\mathbf{g}}(p+q-k, \nu_1+\nu_2-\omega) \times \\ & \{f(\nu_1)f(\nu_2)\bar{f}(\nu_1+\nu_2-\omega) + \bar{f}(\nu_1)\bar{f}(\nu_2)f(\nu_1+\nu_2-\omega)\} \times \\ & (\varepsilon_p + \varepsilon_{k+q-p} + \varepsilon_k + \varepsilon_q + J_{k-p} - u_0) \left\{ \varepsilon_k + \varepsilon_p + \varepsilon_q + \varepsilon_{k+q-p} + \frac{1}{2} (J_{k-p} + J_{k-q}) - u_0 \right\} \end{aligned} \quad (14)$$

$$\begin{aligned} \rho_{\Psi}(k, \omega) = & \frac{1}{N_s^2} \sum_{pq} \int d\nu_1 d\nu_2 \rho_{\mathbf{g}}(p, \nu_1) \rho_{\mathbf{g}}(q, \nu_2) \rho_{\mathbf{g}}(p+q-k, \nu_1+\nu_2-\omega) \times \\ & \{f(\nu_1)f(\nu_2)\bar{f}(\nu_1+\nu_2-\omega) + \bar{f}(\nu_1)\bar{f}(\nu_2)f(\nu_1+\nu_2-\omega)\} \times \\ & (\varepsilon_p + \varepsilon_{k+q-p} + \varepsilon_k + \varepsilon_q + J_{k-p} - u_0), \end{aligned} \quad (15)$$

which differ only through the presence of momentum dependent factors. Here, N_s represents the number of sites on a finite lattice. We discretize the frequency integral into an N_ω fold sum, with a frequency step $\Delta\omega$ so as to cover an interval $|\omega| < 15t$. Typically we choose $N_\omega = 3000$ such that $\Delta\omega = .01t$.

B. Flowchart of the Iterative process

With these equations we can establish an iterative process which leads to a fully selfconsistent spectral function, $\rho_{\mathcal{G}}$. The self consistency loop proceeds as follows.

1. Initialize all quantities to those of the Fermi gas: $\boldsymbol{\mu} = \boldsymbol{\mu}_0$, $\rho_{\Psi} = \rho_{\bar{\Phi}} = 0$, u_0 is set to a plausible value of $2t$.
2. Build $\rho_{\mathbf{g}}$ from latest instance of $\boldsymbol{\mu}$, $\bar{\Phi}$.
3. Calculate $\rho_{\bar{\Phi}}$ from latest instance of $\rho_{\mathbf{g}}$ and u_0 . Obtain the real part via Hilbert transform.
4. Calculate new $\boldsymbol{\mu}$ using a bisection root finder.
5. Repeat steps 2-4 until $\boldsymbol{\mu}$ and $\rho_{\bar{\Phi}}$ have converged to specified tolerance.
6. Calculate ρ_{Ψ} from latest $\rho_{\mathbf{g}}$ and u_0 . Obtain real part through Hilbert transform.
7. Calculate $\sum_k \Psi(k)\mathbf{g}(k)$ and recalculate u_0 with some rootfinder.
8. Return to Step 2 and repeat loop. Continue to the next step only when u_0 has converged to specified tolerance.
9. Calculate $\rho_{\mathcal{G}}$.

The most computationally expensive step in this loop is the double integration for $\rho_{\bar{\Phi}}$. If computed by a direct summation the computational time required will scale as $N_s^2 N_\omega^2$. Furthermore, this slow step is on the innermost loop so it is repeated many times to find selfconsistent values of $\boldsymbol{\mu}$ and u_0 . This leads to unacceptably slow convergence for any reasonable system size. Noting that the summation has the form of a convolution we can make use of FFT routines to calculate $\rho_{\bar{\Phi}}$ with linear scaling in $N_s N_\omega$. This allows us to reach significantly larger systems and lower temperatures than would be possible by a direct approach. The next bottleneck in this flowchart is the calculation of the Hilbert transforms. These can also be made fast through a judicious use of FFT routines. Thus, by using this approach we obtain a scheme which can calculate the full frequency and momentum dependence of $\rho_{\mathcal{G}}$ for lattices of substantial size, $N_s \sim 2000$ at temperatures as low as 30K.

Is it useful to discuss the tolerances set on the Lagrange multipliers. The chemical potential is obtained to a precision of 10^{-5} . This is significantly more accuracy than is required to satisfy the particle sumrule to within a tenth of a percent. However, we find empirically that this strict convergence criterion for $\boldsymbol{\mu}$ can not be satisfied until the spectral function $\rho_{\bar{\Phi}}$ is also well converged. Thus, if $\boldsymbol{\mu}$ has successfully converged to this tolerance we can be sure the $\rho_{\bar{\Phi}}$ is also well converged. The convergence criterion on u_0 requires the sumrule $\sum \Psi(k)g(k) = \frac{n^2}{4}(1 - \frac{n}{2})$ to be satisfied to less than 10^{-4} . Again, this is overkill as it concerns the particle density alone. However, u_0 appears explicitly in $\bar{\Phi}$ and Ψ . The chosen convergence criterion is such the final u_0 lands within .01t of the exact value. This range is comparable to the smallest scales in our calculation, namely the frequency resolution $\Delta\omega$ and an implicit level broadening scale $\eta \rightarrow \Delta\omega$.

To exactly calculate the spectral functions it is important to capture the entire range of the relevant frequencies. For non-interacting Fermions this requires a frequency window no larger than $8t$. However, the spectral functions ρ_Φ and ρ_Ψ have long tails which extend to much higher frequency even though the bare bandwidth is considerably decreased according to Eq. (5). Thus it is important to determine empirically what range of frequency is sufficient to capture the full support of the spectral function. As mentioned before, we employ a frequency grid which extends over the range $|\omega| < 15t$, nearly four times the bare bandwidth, and find that this suffices to capture the support of all functions that arise.

C. Fast Fourier Transforms for evaluating convolutions

We next discuss the strategy used in the computation, where Fast Fourier Transforms (FFT) help reduce the time taken for the task. The equations for $\rho_{\bar{\Phi}}$ and ρ_Ψ have a form which is very similar to the particle-hole bubble diagrams familiar from a 2^{nd} order perturbation treatment of the Hubbard model.

$$\Sigma(k)_{2^{nd}} \sim \sum_{pq} G(p)G(q)G(p+q-k); \quad \Sigma(i,j) \propto G(i,j)^2 G(j,i) \quad (16)$$

where $i = \vec{R}_i, \tau_i$ is a space time point. The convolution in Fourier space is a simple product in the space time domain and hence the real space version is advantageous. This is the well known core idea of the FFT technique, where the time savings arise since the Fourier transforms are performed in $N \log N$ steps rather than N^2 (here $N = N_s \times N_\omega$). The ECFL “self energies”, Ψ and Φ have the same frequency convolution structure of $\Sigma(k)_{2^{nd}}$ which appears only through the frequency arguments of \mathbf{g} . However, the $\rho_{\bar{\Phi}}$ and ρ_Ψ equations suffer from the presence of momentum-dependent decorations which render them not technically convolutions. Nonetheless we can use FFT routines to solve these summations. The strategy is to break up the integral into elementary pieces that do have the form of a convolution. We then avoid the need to do one large integral with quadratic complexity by doing many (≈ 70) small FFT’s of linear complexity.

To accomplish this we define several correlation functions which are similar to particle-hole bubbles.

$$\begin{aligned} \chi_0(Q) &= \sum_q \mathbf{g}(q)\mathbf{g}(q+Q); & \chi_1(Q) &= \sum_q \varepsilon_q \mathbf{g}(q)\mathbf{g}(q+Q) \\ \chi_2(Q) &= \sum_q \varepsilon_{q+Q} \mathbf{g}(q)\mathbf{g}(q+Q); & \chi_3(Q) &= \sum_q \varepsilon_{q+Q}^2 \mathbf{g}(q)\mathbf{g}(q+Q) \end{aligned} \quad (17)$$

each of which is a full convolution in frequency and momentum and has a spectral function which can be calculated by FFT in linear time.

With these correlation functions every $\mathbf{g}\mathbf{g}\mathbf{g}$ term (except one to be discussed later) found in Eq. (3) and Eq. (6) can be written in the form

$$B_{\mathbf{g}\mathbf{g}\mathbf{g}}(k) = F_1(k) \sum_p F_2(p) \mathbf{g}(p) \chi_n(p-k) F_3(p-k). \quad (18)$$

where F_1, F_2 , and F_3 are each functions of momentum only and their arguments are carefully matched with the arguments of $B_{\mathbf{g}\mathbf{g}\mathbf{g}}$, \mathbf{g} , and χ_n as they appear in the integral such that all factors fit the form of a convolution. In this way we can massage every term of $\rho_{\bar{\Phi}}$ into a convolution of one \mathbf{g} and a χ_n rather than three \mathbf{g} ’s as originally written. There is one term in this problem which cannot be treated in this way because the argument matching of Eq. (18) cannot be achieved in such a simple way. This term looks like

$$\bar{\Phi}_{JJ}(k) = \sum_{pq} J_{q-k} J_{p-k} \mathbf{g}(p) \mathbf{g}(q) \mathbf{g}(p+q-k)$$

Nonetheless, this problematic term can be treated by the FFT approach if the factor J_{q-k} is broken up using angle addition identities. That the function J_k can be decomposed into a small number of Fourier components is a consequence of the locality of the exchange interaction.

In defining the Fourier transforms, we need to extend the frequency functions to infinity, since it is only then that the frequency convolutions become products in the time domain. Recall that our frequency integrals have been discretized onto N_ω frequency bins which cover the support of our spectral functions. In extending the discretized

frequency summations to infinity, we follow the standard procedure of padding the N_ω frequency bins with an equal number of frequency bins with value zero. By a simple exercise one can verify that padding finite data in this way allows an application of the periodic FFT in such a way that the result of the infinite transform is reproduced. This procedure is discussed in²². No such considerations are required for the momentum sums which are by definition periodic and discrete, making them naturally suited to treatment by FFT.

The Hilbert transform Eq. (10) is formally a convolution and can therefore be solved with the advantages of the FFT routines. Once again, however, we face the problem that this convolution is a non-periodic frequency integral. Furthermore, the Hilbert kernel $\frac{1}{\omega}$, unlike other spectral functions with a compact support, falls off very slowly at large frequencies so the padding trick from the $\mathbf{g}\chi$ -convolution will not work well in this case. It is found that the use of FFT's to calculate a Hilbert transform will always introduce some error. Fortunately, this error can be controlled by increasing the length of padding used. In our code we use a frequency padding of $8N_\omega$ for the Hilbert transforms. This relegates the error of the real parts of the various functions to very high frequency, far beyond the compact support of the spectral functions. The error introduced is therefore negligible.

IV. RESULTS

A. Physical Variables

The program includes several parameters which can be varied. These include the tight binding bandstructure (through hopping parameters t , t' etc.), the spin coupling J , density, and temperature. For the parameters of the model, we study two important situations:

- **Case (A)** the nearest neighbor hopping model with $t \sim 3000K$ and $J \sim 900K$;
- **Case (B)** with $t' = -.4t$ and the other parameters unchanged.

Case (A) is the most natural one to study since it is minimal. However at the bare level, its Fermi surface near half filling remains closed around the $\Gamma = (0,0)$ point in the Brillouin zone. This is in contrast to angle resolved photoemission (ARPES) reconstructed Fermi surfaces in say *BISSCO* that open up, i.e. no longer surround the Γ point becoming hole like. For this reason we study the Case (B) as well, with a Fermi surface that closes around the Γ point for $n \lesssim .55$ and opens up at higher n . The Fermi momentum along the $\langle 11 \rangle$ direction is measured at $n \sim .85$ in experiments on *BISSCO* as $\sim .43\text{\AA}^{-1}$ and provides a useful check on the parameters. Within the Case (A) we find a considerably larger value $\sim .55\text{\AA}^{-1}$ while Case (B) gives a better fit $\sim .45\text{\AA}^{-1}$. While the Fermi volume is conserved by the theory reported here, the shape of the Fermi surface can, in principle, change since the self energy $\bar{\Phi}(k)$ depends upon the wave vector \vec{k} , so these numbers may in principle change somewhat in the final spectrum. However, in this $O(\lambda^2)$ calculation we find that the “bare” Fermi surface is preserved to high accuracy.

We also note that for **Case (B)**, the band density of states has a van Hove singularity (vHs) close to the bare Fermi energy for density $n \sim .58$. This ends up influencing the results for this case significantly in a range of densities around .6, and the contrast between this and **Case (A)** gives an idea of the role played by the van Hove points.

B. Other parameters in the programs

The code can furthermore be implemented on lattices of different size and spatial dimension. For a given choice of these parameters an appropriate choice must be made for computational grid. This includes the lattice size as well as the discretized frequency grid. We have looked at converged spectral functions for a wide variety of these parameters.

The majority of the following results were performed on a square lattice which has dimension $L \times L$ where $L=36$ and the lattice is taken to have periodic boundary conditions and translational symmetry. We therefore work in a momentum representation with an $L \times L$ sized k -grid of points $k_{i,j} = \frac{\pi}{aL}(i,j)$ where $1 \leq i,j \leq L$ and a is the lattice parameter, taken to be $a = 3.82\text{\AA}$. The spectral functions have compact support which extends to $|\omega| \lesssim 2Zt$. We choose a frequency range $|\omega| < 15t = \omega_c/2$ which is sufficient to capture the full range of the spectral functions. We discretize this frequency range in $N_\omega = 3000$ bins each of width $\Delta\omega = \frac{\omega_c}{N_\omega} = .01t$. $\Delta\omega$ is the lowest resolvable frequency scale in the calculation so it is prudent to disallow any spectral features from becoming any sharper than this scale. Therefore we introduce the convergence factor $\eta_{min} = \Delta\omega$ which will act as a lower limit on the width of spectral features. Thus in the Dysonian form of $\rho_{\mathbf{g}}$ Eq. (13) we set $\rho_{\bar{\Phi}} \rightarrow \rho_{\bar{\Phi}} + \frac{\eta}{\pi}$. It is however reasonable to include larger η in the calculation to imitate the effects of impurity scattering events in ARPES experiments. This parameter has been discussed previously in Ref. (2).

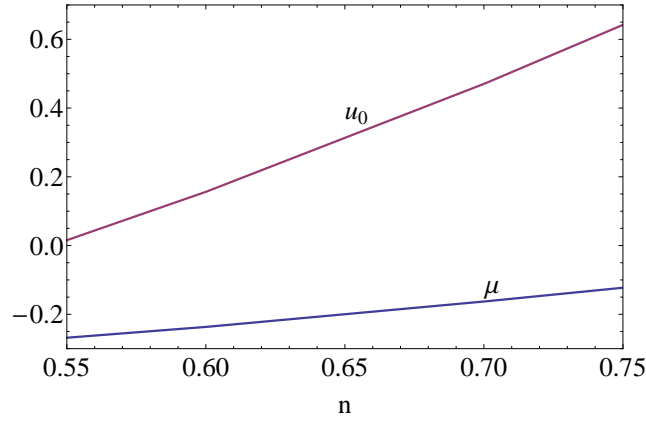


FIG. 1: Case (B) $T = 130K$. The density of dependence of the two Lagrange multipliers, μ and u_0 in eV. This density dependence is similar in character to that found for different choices of (J, t', T) . The chemical potential approaches 0 zero from below. This agrees with the expectation that $\mu = 0$ at half filling. u_0 is rising monotonically with density. The interpretation of this behavior is that with increased density, this $O(\lambda^2)$ theory is unable to prevent double occupancy entirely. Thus the finite u_0 (in effect, a repulsive Hubbard U) must reenter the problem to penalize doubly occupied states. The scale of u_0 is comparable to the renormalized bandwidth ($\approx 1eV$).

C. Thermodynamics

In Fig. (1) we display the density dependence of the two Lagrange multipliers, μ and u_0 , namely the chemical potential, and the effective Coulomb energy for the auxiliary Fermions generated by the self consistency condition. The temperature dependence of μ is shown below in Fig. (2) revealing the temperature scale for the thermodynamics of the ECFL. For a Fermi liquid we expect that the chemical potential goes as $\mu(T) = \mu_0 - bT^2$. We define a Temperature scale T_μ which sets the strength of the $O(T^2)$ term according to

$$T_\mu = \sqrt{\left| \frac{\mu_0}{b} \right|}. \quad (19)$$

The temperature dependence of μ is plotted in Fig. (2) for Cases (A) and (B). Case (A) exhibits the expected quadratic dependence at low T at all densities up to the highest allowed by the $O(\lambda^2)$ approximation. T_μ has been extracted and plotted in the inset as a function of the density n . However, in Case (B) the chemical potential sits very close to a van Hove singularity (vHs) in the very overdoped regime. Consequently, the quadratic form of $\mu(T)$ is disturbed and we do not attempt to extract a T_μ for this case. The density of states of Case (B) is shown in the inset to illustrate the presence of the vHs at low frequency. Note the reduction of the scale of T_μ in Case (A) as we approach half filling, i.e. as the chemical potential approaches a vHs.

The temperature dependence of $u_0(T)$ (shown as an inset of Fig. (2)) differs from $\mu(T)$ in several ways. Whereas the quadratic dependence of the chemical dependence occurs because of marginal changes in the occupation only at low frequency, u_0 is explicitly present in the form of Φ and Ψ so small changes in u_0 are felt at all frequencies. In the high temperature limit u_0 acquires a linear temperature dependence (like μ) and the low temperature dependence is also linear, these are separated by a minimum at an intermediate T scale that it is larger in Case(B) than in Case (A).

D. Frequency independent Variables

We now proceed to study the Fermi surface in this theory through the momentum occupation function

$$m_k = \sum_{\omega_n} \mathcal{G}(k, i\omega_n) e^{i\omega_n 0^+}. \quad (20)$$

A drop in this function at the Fermi surface helps to locate the latter. This can be compared with the “Luttinger surface” defined by a sign change in $\text{Re}\mathcal{G}(k, 0)$ given in terms of the spectral function by

$$\text{Re } \mathcal{G}(\vec{k}, 0) = \int_{-\infty}^{\infty} \frac{\rho_{\mathbf{g}}(\vec{k}, \nu) d\nu}{\nu} \quad (21)$$

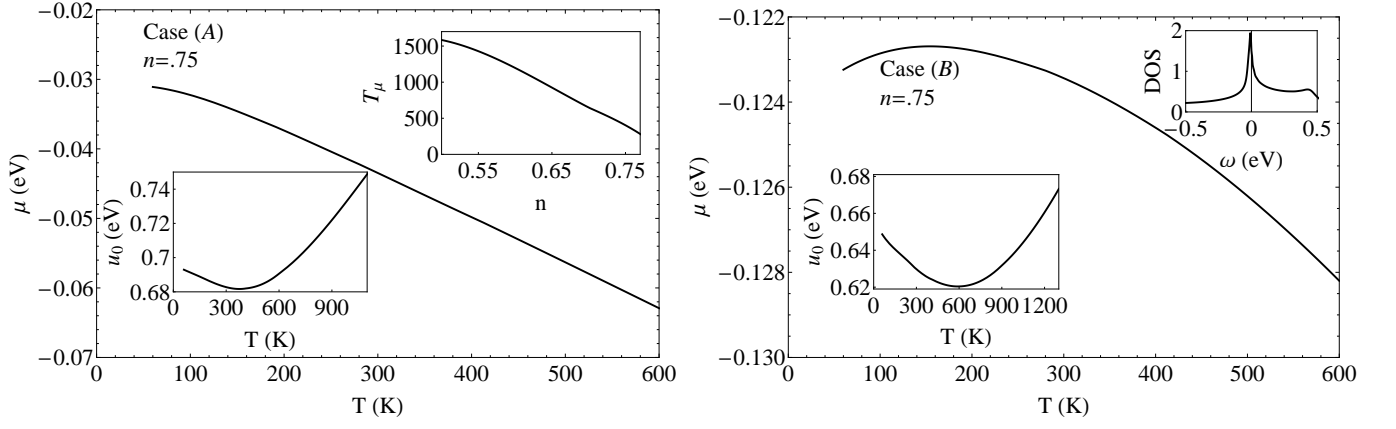


FIG. 2: The chemical potential μ versus T at $n = .75$ for Cases (A) and (B) (left and right respectively). An effective Fermi temperature T_μ , found from Eq. (19), is shown in Case (A) as a function of the density. In Case (B) the DOS of states is shown as an inset to illustrate the vHs. Note that the scale of variation of the chemical potential $\Delta\mu \sim 15$ meV in heating from $T = 100$ K to $T = 300$ K, is quite large as compared to the changes that occur in weakly correlated matter, and are potentially observable in ARPES. A shrunk overall energy scale, seen clearly in Fig. (5), is ultimately responsible for this sensitivity. The temperature dependence of u_0 is shown in each case to be non-monotonic with a minimum at finite temperature. At high temperature u_0 rises linearly with T , similarly to μ .

At $T = 0$ the Fermi surface in \vec{k} space is traced out by $\text{Re } \mathcal{G}^{-1}(\vec{k}, 0) = 0$, as dictated by the Luttinger Ward sum rule or the volume theorem. In Fig. (3) is plotted the momentum distribution m_k at $T = 130$ K for various densities of Cases (A) and (B) along three principle directions of the Brillouin zone. The Luttinger Ward zero crossings $\text{Re } \mathcal{G}^{-1}(\vec{k}, 0) = 0$ are depicted by dashed vertical lines. There is a close correspondence between these crossings and the point where $m_k = .5$, similarly to that noted previously by Stephan and Horsch⁹ in an exact diagonalization study. Since this correspondence is not on any rigorously firm basis, it is difficult to do more than to list the conditions for its approximate validity. Using high temperature expansions for the t - J model Singh and Glenister¹⁰ found the Fermi surface to be that of the Fermi gas by various criteria, and noted that the condition $m_{k_F} \sim 0.5$ is only satisfied approximately at high T . In Fig. (4) we find that at higher temperature where the QP near the Fermi surface have been significantly broadened, and thus there are deviations from $m_{k_F} \sim 0.5$ in Case (B), although Case(A) has much smaller deviations. In Fig. (3) and Fig. (4), a point of considerable interest is the spill over of the occupation to the

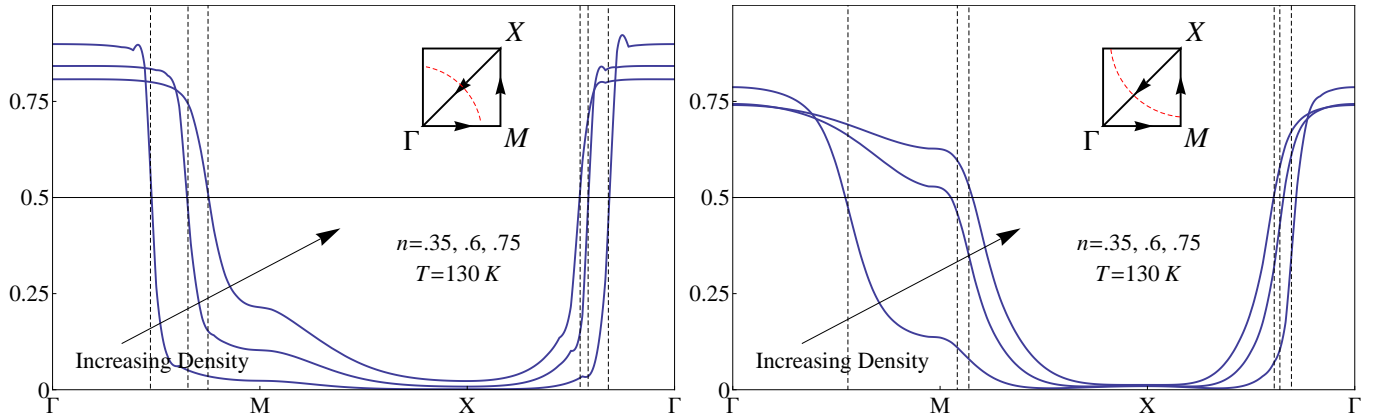


FIG. 3: The quasiparticle occupation m_k is plotted along three principle lines of the Brillouin zone with $T = 130$ K. The panel on the left shows Case (A) with a Fermi surface that is closed around $k = (0, 0)$. Case (B) is shown in the right panel and has an open Fermi surface due to the presence of the finite t' . In each case the FS is the same as in the non-interacting problem. The Luttinger Ward crossing $\text{Re } \mathcal{G}^{-1}(\vec{k}, 0) = 0$ is indicated for each density by the vertical dashed lines. For each density and each bandstructure the Luttinger Ward crossings correspond well with the condition $m_k = 1/2$. Case (A) shows much more variation as a function of density, because the gradient of ε_k is relatively small in the vicinity of the M-point.

regions in k space that are unoccupied in the Fermi gas- as noted in various variational wave function studies of the

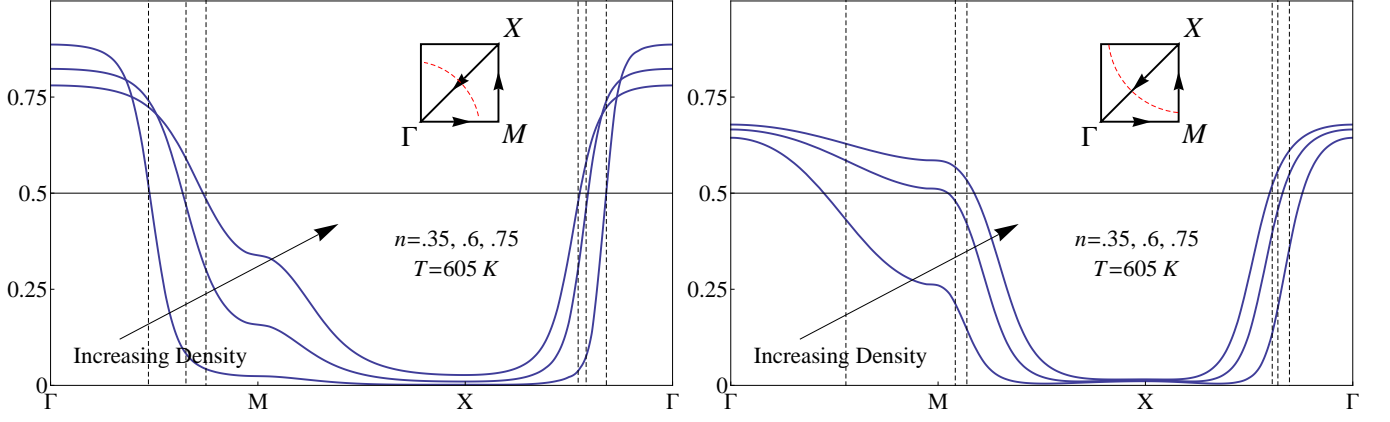


FIG. 4: The quasiparticle occupation function m_k is plotted along principle lines of the Brillouin zone for $T = 605K$. Unlike Fig. (3), the condition $m_{k_F} = 1/2$ is not satisfied closely in Case (B), although it is applicable to reasonable precision for Case (A).

t - J model already^{15–17}. At each k value, since Eq. (20) can be written as a sum rule

$$m_k = \int \rho_G(k, \omega) f(\omega) d\omega, \quad (22)$$

we see that for momenta $k > k_F$, the spill over variable m_k provides an estimate of the spectral weight $\rho_G(k, \omega)$ at energies below the chemical potential, and should be of help in disentangling or resolving the “background” often seen but discarded in ARPES studies.

E. Quasiparticle Dispersion and Z_k

We next study the location of the quasiparticle peaks. We can study three interesting functions to get a clear idea of the many body renormalizations that effect the dispersion relations in this theory.

$$\begin{aligned} \bar{\epsilon}_k &= \left(1 - n + \frac{3n^2}{8}\right) \epsilon_k + \frac{1}{2} \sum_q J_{k-q} m_q \\ E_k &= \bar{\epsilon}_k - \mu + \text{Re } \bar{\Phi}(k, E_k) \\ E_k^* &= \max[\rho_G(k, \omega) : \omega], \end{aligned} \quad (23)$$

where Eq. (5) defines the “bare energy” with its static renormalization. Below we drop the J -term, which is quite small, $O(1/20)$. Further E_k locates the peak of the auxiliary Greens function \mathbf{g} , and E_k^* locates the peak of the physical Greens function \mathcal{G} . This dispersion is complementary to E_k^* from Eq. (23). E_k^* in Eq. (23) is the dispersion from the Energy Distribution Curve (EDC). Thus E_k and E_k^* give us the energies of the auxiliary Fermions and the physical Fermions. The theory has a strong asymmetry in the line shapes as noted in Ref. (3), and hence it is also interesting to track separately the locations of the left and right half maxima. In Fig. (5) we illustrate the density dependence of the three dispersions in Eq. (23) for Cases (A) and (B). Furthermore, we provide insets which the bandwidths, $W(n)$, of the various dispersions as a function of the density. Note the the bare dispersion of ϵ_k is 2eV for both cases. In Fig. (6) we plot the dispersions E_k and E_k^* along with the asymmetric half maxima at a single density, $n = .75$. Near the Fermi surface we see that $E_k \approx E_k^*$ but they differ far from the Fermi surface where the lineshapes become more extremely skewed.

We next explore the difference between E_k and E_k^* near the bottom of the band (Fig. (5)). The feature is reminiscent of the “high energy kink”, or more picturesquely “the waterfall” observed in the Cuprate compounds²⁴ and we next relate this to specific features of the spectral function. To do so it is useful to plot the Momentum Distribution Curve (MDC) dispersion $E_{MDC}(k)$ found by locating the maxima in \vec{k} at a fixed energy ω

$$k^*(\omega) = \max[\rho_G(k, \omega) : k], \quad E_{MDC}(k) = \text{Inverse of } k^*(E). \quad (24)$$

The dispersion $E_{MDC}(k)$ can be compared with the energies in Eq. (23). In Fig. (7) the spectral function is depicted as a color density plot. Near the Γ -point where $k = (0, 0)$ the QP becomes incoherent and the bulk of its spectral

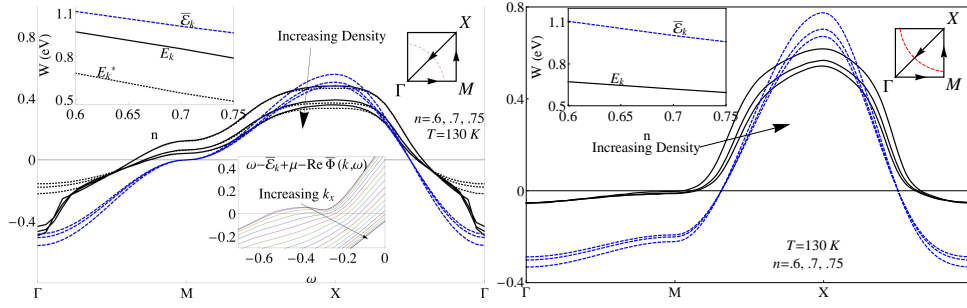


FIG. 5: $T = 130K$. The vertical energy scale is in eV. The three dispersions defined in Eq. (23) are plotted along principle directions for three different densities. The insets show the bandwidth of the dispersions as a function of the density. The bare bandwidth is 2eV but each of these dispersions shrinks to a smaller bandwidth. Here $\bar{\epsilon}_k$ is a k-independent scaling of the bare dispersion. The bandwidth renormalization due to $\text{Re}\Phi$ in Eq. (23) is k-dependent, and so E_k has a different shape than ϵ_k . Note that $E_k \sim E_k^*$ near the Fermi surface. However, in Case (A) E_k^* differs from E_k near the Γ -point for each of the densities. A lower inset on the left panel shows the evolution of real part of the denominator of $\mathbf{g}(k, \omega)$ with ω to illustrate the behavior of E_k^* . A non-monotonic feature develops with a minimum near $\omega = -3\text{eV}$ which corresponds to the peak E_k^* . This peak disperses smoothly into E_k at higher k. However, E_k has a kink at small k where it disperses downward sharply. The pole E_k then acquires a wide peak which is short and broad.

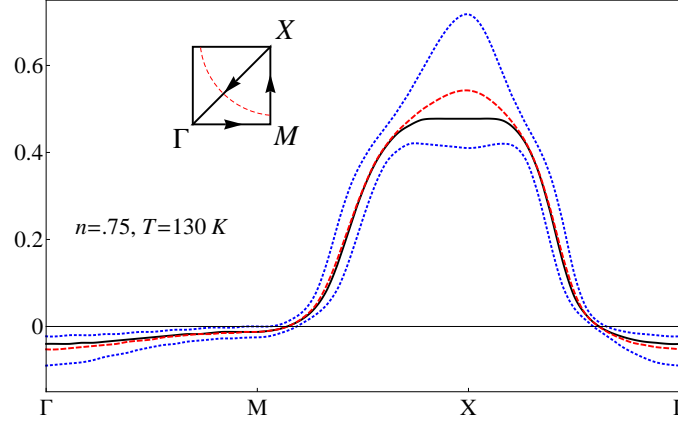


FIG. 6: Case(B) $T = 130K$ We plot the physical quasiparticle dispersion E_k^* (Black solid) and the location of the two half maxima (Blue Dotted), as well as the auxiliary Fermion dispersion energy E_k from Eq. (23) (Red Dashed). The skew in the lineshapes of the physical particles leads to the nonsymmetric location of the black line relative to the blue dotted lines.

weight is spread out to high negative frequencies. In this region the MDC peaks differ from E_k and E_k^* . This is the operational definition of the waterfall as seen in the Cuprates. The scales of the waterfall in this calculation are both slightly smaller than those seen in the Cuprates. The MDC curve recovers the scale of the bare dispersion ϵ_k .

Within this theory we can explore of various parameter dependences of the waterfall anomaly. In Fig. (8) we show density plots of the spectral function with negative and positive t'/t . These correspond to Case (B) and a third case with $t'/t = .4$ which can be identified with the phenomenology of the electron doped Cuprates. In these plots we can see two major trends in the development of the high energy features of the spectral function. Firstly, the waterfall of the electron doped case is larger than that of Case(A) by a factor of 2. Case (B) has no measurable waterfall; the background at negative frequency is essentially featureless near the Γ -point. Meanwhile at positive frequencies, a similar feature develops near $k = (\pi, \pi)$ as t'/t is decreased. Case (B) shows the best example of this inverted waterfall. Case (A) is an intermediate example where both features are present. The location, direction and magnitude of the waterfall is correlated with the points of high curvature of the dispersion. Regions where the QP band is relatively flat show agreement between E_{MDC} and E_{EDC} . The waterfall is also visible, albeit with a decreased magnitude, at much lower density.

We can also study the Fermi velocity along a given Fermi surface. In Fig. (9) the angle dependence of the Fermi velocity is plotted over an eighth of the Brillouin zone for Cases (A) and (B). Case (A) shows a significant increase by a factor of 2 in velocity as we move from the antinodal to nodal directions. The absolute values of the velocities are roughly similar to those seen in experiments.

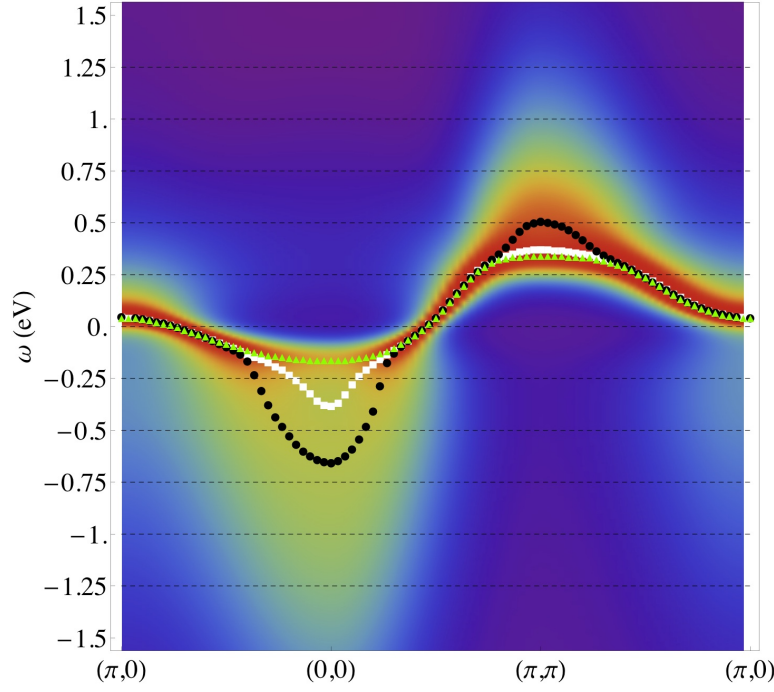


FIG. 7: $L = 60$, $(n, T) = (.75, 300K)$. The spectral function of Case (A) is presented as a density plot to illustrate the structure of the background spectrum. We have overlaid the E_k , E_k^* , and $E_{MDC}(k)$ spectra as white, green and black points, respectively. In the low frequency region near k_F we see that the MDC, EDC, and E_k peaks coincide. Of particular interest however, is the region near $k = (0, 0)$ where the MDC peaks occur at a significantly higher scale than E_k or E_k^* . Furthermore, in this region the EDC peak loses weight. Notice that the red peaks of the density plot, representing a sharp QP band, fade out to yellow near the Γ -point. This pronounced difference between the EDC and MDC peaks indicates that a waterfall-like phenomenon is present in this theory. There is also a new feature at positive frequency near $k = (\pi, \pi)$ which looks waterfall-like. This is explored further below in Fig. (8).

Finally we want to know the QP weight at the Fermi surface. In a conventional Fermi liquid the QP weight is defined by

$$Z_k = \frac{1}{1 - \frac{\partial \Sigma}{\partial \omega}}$$

where Σ is the Dysonian Self energy and Z_k should be evaluated at $(k, \omega) = (k_F, 0)$. This definition does not immediately work for us as we do not have a conventional Dysonian form for our \mathcal{G} . To obtain an equivalent definition for Z_k we define a new self energy according to the form

$$\mathcal{G} = \frac{A + \Psi}{x - \Phi} = \frac{A}{x - \Sigma} \quad (25)$$

where in this approximation $A = 1 - \frac{n}{2} + \frac{n^2}{4}$ and $x = i\omega + \mu - \bar{\epsilon}_k$. In analogy to the standard FL we now define

$$Z_k = \frac{A}{1 - \frac{\partial \Sigma}{\partial \omega}}. \quad (26)$$

Note that A differs from $1 - \frac{n}{2}$ owing to the second order in λ approximation made here. While it may be tempting to drop the term A from Eq. (26), it represents an important piece of physics in the larger context and therefore must be retained. To see this, note that the full spectral function of canonical electrons, e.g. in a large U Hubbard model, would have features at the scale of U that correspond to the upper Hubbard band, and are thrown out in the t - J model, where we have isolated the lower Hubbard band. Thus in a comprehensive canonical theory, the (low) value of Z_k should be imagined to be compensated by a large piece $1 - Z_k$ that is partly in the lower Hubbard band, and also partly in the upper Hubbard band (outside the domain of the t - J model). Numerics are performed at finite

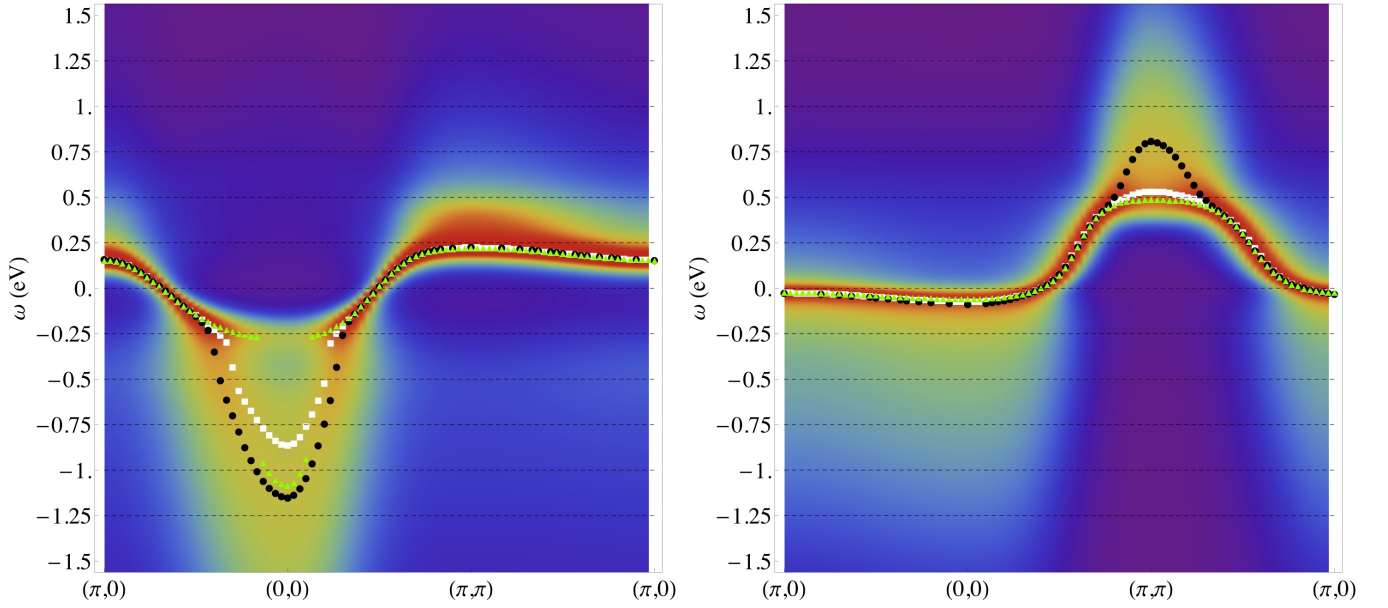


FIG. 8: $L = 60$, $(n, T) = (.75, 300K)$. The left and right plots show $t'/t = .4$ and $t'/t = -.4$, demonstrating that the background and the kink feature are sensitive to the bare band parameters. In these plots we overlay three dispersions to help with the visualization of the kinks. These are E_{MDC} , E_k , and E_k^* (this is identical to E_{EDC}) in respectively black, white, green. A positive t' (usually associated with electron doping) results in the largest binding energy scale for the kink anomaly near the Γ -point. This feature shrinks as t' is decreased. Therefore this calculation suggests that the relative magnitude of the waterfall in hole and electron doped Cuprates is a consequence of the sign of t' , a result similar to the Hubbard model QMC results of Ref. (18). Simultaneously, a reciprocal kink at positive frequency, which we might call a waterspout, occurs around $k = (\pi, \pi)$ with increasing magnitude for lower t' . This feature is therefore predicted by this calculation for future inverse photoemission studies.

temperature and the $T=0$ value of $\frac{\partial \Sigma}{\partial \omega}$ is obtained by extrapolating the finite T data. It is found that Z_k falls quickly with density in both Cases (A) and (B) as plotted in Fig. (10). At the highest densities, Z_k is lower for Case (B) but it falls more abruptly at low densities in Case (A). It is clear that such small values of Z_k speak of enormous backgrounds in the spectral functions, and below we capture the energy dependence of these backgrounds in detail.

F. Self energies

We now display the self energies that are involved in calculating the spectral functions. In Fig. (11) we show $\rho_{\overline{\Phi}}$ and ρ_{Ψ} . Both functions exhibit the ω^2 behavior very close to zero, as expected of a Fermi liquid self energy. Unlike conventional Fermi liquids (such as the 2^{nd} order perturbation theory treatment of the Hubbard model), the magnitude of the quadratic term is strongly k -dependent. From these functions and the associated real parts we can construct a Dyson self energy as defined earlier in Eq. (25). In Fig. (12) we plot the computed the imaginary part of the Dyson self energy ρ_{Σ} . It exhibits a similar magnitude and k -dependence at low frequency to that in $\rho_{\overline{\Phi}}$. However, asymmetries begin to appear at intermediate frequencies. It is remarkable that at positive energy the function is considerably smaller than at negative energies, a feature that has already been noted in Ref. (3) and also in recent work in Ref. (21).

The right panel of Fig. (12) shows low frequency fit parameters of ρ_{Σ} as a function of k . An appreciable low frequency asymmetry develops for unoccupied k . At higher frequency much larger asymmetries arise. Specifically, we see that for negative frequencies, a large scattering lobe extends outward to $-\omega \approx 3eV$ with considerable weight. This feature is larger for occupied wavevectors. No analogous feature appears for positive frequency. In Fig. (13) we show the T dependence of the single particle relaxation, obtained from the decay rate of the Dyson self energy at the quasiparticle pole $\text{Im}\Sigma$. The Case (B) is clearly unusual, but becomes understandable when we recall the proximity of the van Hove point near the Fermi energy for $n \sim .58$. Case (A) shows a crossover at about ~ 150 K to linear in T behavior, as compared to $T_{\mu} \sim 400$ K discussed above in Fig. (2). These scales are lower than would be found in the 2^{nd} order treatment of the Hubbard model by roughly a factor of two (at this density). This difference arises because

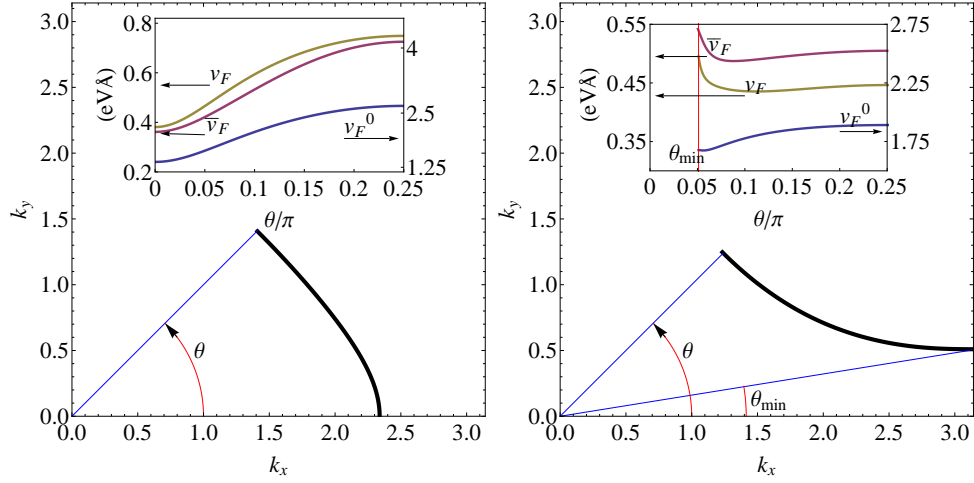


FIG. 9: The Fermi surface and Fermi velocities for Cases (A) and (B) (left and right) with $n = .75$. The FS is marked out in a minimal octant of the square lattice. The gradients of the various dispersions ($\varepsilon_k, \bar{\varepsilon}_k, E_k$) evaluated at the FS are called (v_F^0, \bar{v}_F, v_F). In Ref. (23) the Fermi velocity of *optimally doped* BISSCO is measured as being nearly independent of the angle θ and has a value of $1.8 \pm .2 \text{ eV}\text{\AA}$, i.e. larger than ours (with our scale $t \sim .25 \text{ eV}$) by factor of 3 to 4.

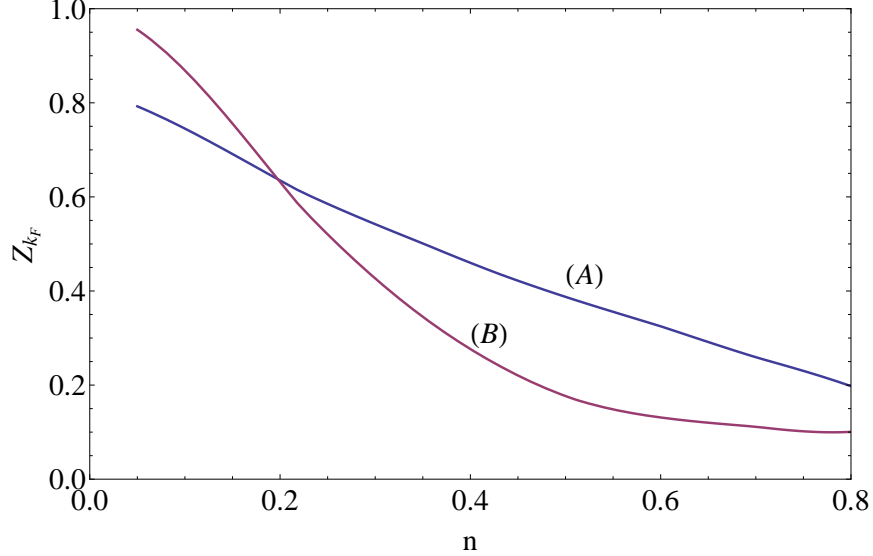


FIG. 10: The quasiparticle weight Z_{k_F} is plotted as a function of density for Cases (A) and (B). In each case Z_{k_F} vanishes with increased density, more quickly in Case (B), due to the vHs at $n \sim .58$. The incoherent spectral contribution is therefore already ~ 4 times greater than the quasiparticle part at $n \sim .7$, and this ratio appears to increase further near half filling.

of the bandwidth reduction which increases the important ratio T/W . Thus the rather early crossover is not caused by the large incoherent contributions to the Greens functions which arise in the $O(\lambda^2)$. It is actually an effect of the $O(\lambda)$ terms.

G. Spectral Functions and ARPES Lineshapes

In this section, we present our results for the spectral functions within the second order theory to $O(\lambda^2)$, argued above to be valid for low (high) enough particle (hole) density, say $n \lesssim 0.7$. In earlier work Ref. (2), we have compared the approximate results of the ECFL formalism with some phenomenological inputs, with the experimental data at somewhat higher particle densities $n \sim 0.85$. Ref. (2) found remarkably good fits with the line shapes in the nodal direction. We are content in this work to present the results from a microscopic calculation of ECFL with the simple

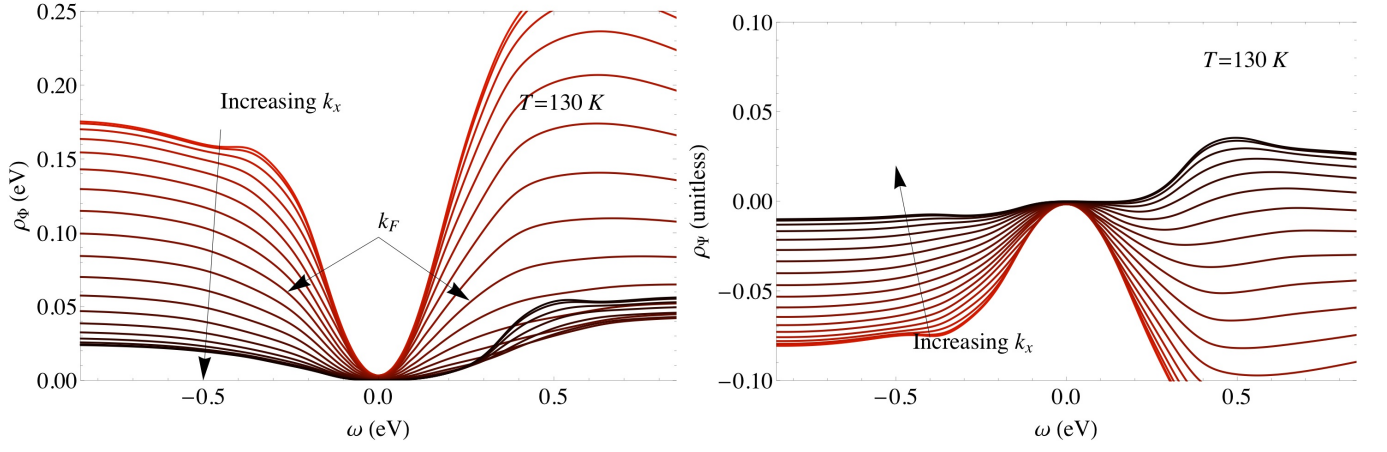


FIG. 11: Case (A) with $(n, T) = (.75, 130K)$. The spectral functions for the two self energies Φ and Ψ , i.e. ρ_{Φ} (left) and ρ_{Ψ} (right) in the two panels at several k points along the $\langle 11 \rangle$ direction vs. frequency. Both are roughly quadratic and symmetric at low frequency, but have a strongly k -dependent curvature. In the plot of ρ_{Φ} , the minimum width η chops off the bottom of the low frequency minimum.

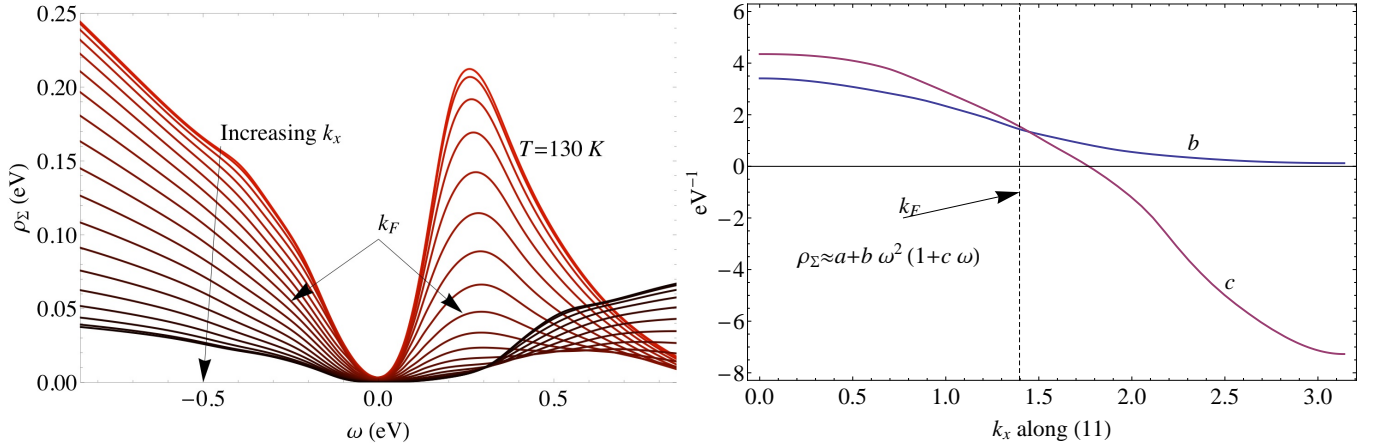


FIG. 12: Case (A) with $(n, T) = (.75, 130K)$. The Dyson self energy Σ can be inferred from the Greens function as in Eq. (25), and its spectral function ρ_{Σ} displayed at several k points along the $\langle 11 \rangle$ direction vs. frequency. As with ρ_{Φ} , ρ_{Σ} has inherited a strong k dependence. We note here that the primary k -dependence at low frequency is seen in the softening of the quadratic coefficient with increased k . There is also an asymmetric term cubic term $\rho_{\Sigma} \propto \omega^3$ which grows in magnitude with increasing k beyond k_F , as one sees from the panel at right, where we also see that in the occupied portion of the Brillouin zone $k < k_F$ the curvature and cubic term have relatively little k -dependence.

band dispersions in Case (A) and Case (B), at lower particle densities. We note below that the line shapes obtained here are of the same general nature as the ones in Ref. (2), although as one expects from a lower density situation, we find somewhat less dynamical asymmetry about zero energy. More detailed comparison with data near optimal doping with the microscopic ECFL theory must await the solution of the third or higher order equations where the criterion for validity discussed above (see para following Eq. (8)) is satisfied more closely than here.

Let us first note the local density of states at density (LDOS) $n = 0.75$ for both cases at low T in Fig. (14). We note that the chemical potential is rather close to the peak in the LDOS for Case (B) at these fillings, and this proximity influences the results for this case significantly.

We begin by displaying the spectral lines at very low density of particles in Fig. (15), where the spectral lines for $k < k_F$ begin to show a characteristic tails at high binding energy relative to the lines at $k > k_F$, which are more Lorentzian. Also interesting is the sharpening of the lines at higher momenta $k \gg k_F$, suggesting longer lived quasiparticles far outside the FS, in parallel to the results in Ref. (21).

We next display in a set of figures Fig.(16) to Fig. (19) the spectral functions of the theory at low and high temperatures, at different densities, and along different directions. The first panel Fig. (16) shows the nodal spectral functions of Cases (A) and (B) at three different temperatures. The lines are quite sharp near k_F but broaden out

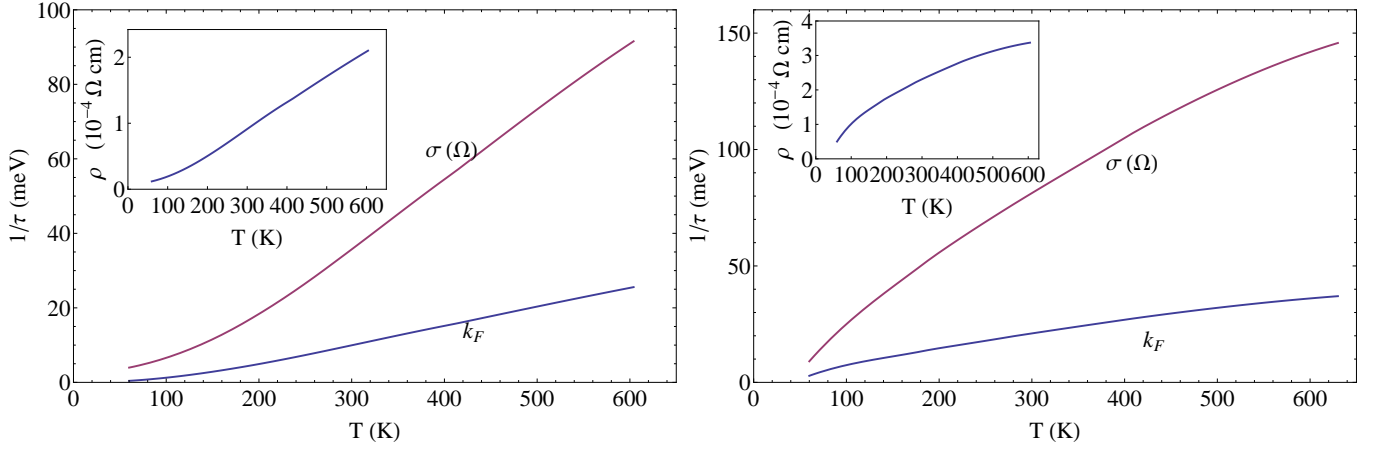


FIG. 13: Case (B). The inverse lifetimes for QP's at the Fermi surface along $\langle 11 \rangle$ obtained from the imaginary part of the Dyson self energy, as a function of temperature, along with the momentum averaged inverse lifetime obtained from the optical conductivity as in Eq. (28). The temperature dependence is more linear than would be expected of a Fermi liquid with an early onset, caused by the shrinking band width as seen directly in Fig. (5). This situation in Case (B) appears even less FL-like due to the vHs.

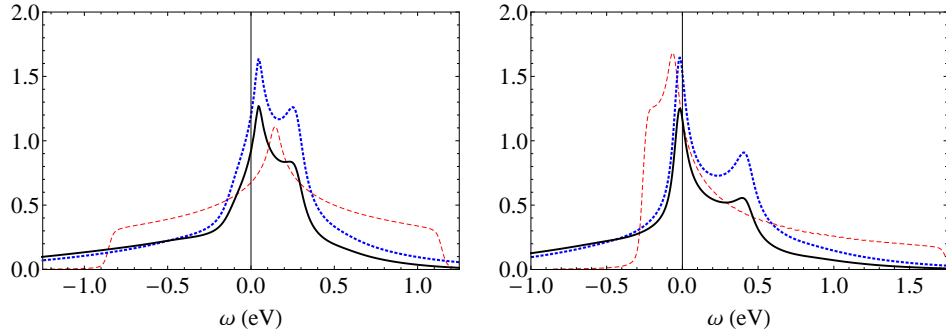


FIG. 14: For Cases (A) and (B) (left and right) with $n = .75$, we display the local density of states. The LDOS of the physical \mathcal{G} is shown in black while the bare DOS is the dashed red curve. The LDOS of the auxiliary \mathbf{g} is shown as a dotted blue curve. The quasiparticle bandwidth is considerably more narrow and in each case there is a long tail extending to large negative frequency. Furthermore, it is clear that the tail of \mathcal{G} decays more slowly (quickly) than \mathbf{g} for large negative (positive) frequencies. This arises from the asymmetry produced by the caparison factor.

rapidly away from k_F . The insets give an idea of the change of spectral density with T . It is interesting that the detailed shapes at higher binding energy differ between the two cases, with Case (A) showing a more pronounced tendency for a rise with (binding) energy, giving rise to a minimum in some cases. This was also noted in Eq. (5) in the discussion of the difference between E_k and E_k^* . A feature of this kind has been observed in^{2,4} and is reminiscent of asymmetrical features seen in ARPES experiment of LSCO. For Case (A) it is also noteworthy that lines for $k > k_F$ are sharper than the ones inside, and further, have tails that extend into $\omega \leq 0$, thereby contributing to what is commonly relegated as “noise” or “background” in ARPES.

Both Case (A) and Case (B) exhibit an interesting behavior in the QP scattering rates. This is seen in Fig. (17) over the first quadrant of the Brillouin zone. We plot the decay rate from the Dysonian self energy: $\Gamma_k = \rho_\Sigma(k, E_k)$ as a function of \vec{k} in Fig. (17). It is clear that in both cases there is a surface of minimum scattering rate which coincides with the Fermi surface. However, there is a second surface with $k > k_F$, where the scattering rates are a local minimum. This feature is particularly strong in Case (B) and can be seen clearly in the lineshapes of Fig. (16) and even at the very low density spectral function seen in Fig. (15). In Case (A) the feature is less pronounced but is nonetheless present.

We next discuss the role of elastic scattering in the lineshapes following Ref. (2). As discussed in² the parameter η can be used to model the effects of impurity scattering upon ARPES spectra and has invoked to distinguish between laser ARPES and synchrotron ARPES. Using fits from² we arrive at $\eta = .032\text{eV}$ and $\eta = .12\text{eV}$ as being the typical values for describing the ARPES lineshapes of laser and synchrotron ARPES respectively. It is therefore interesting

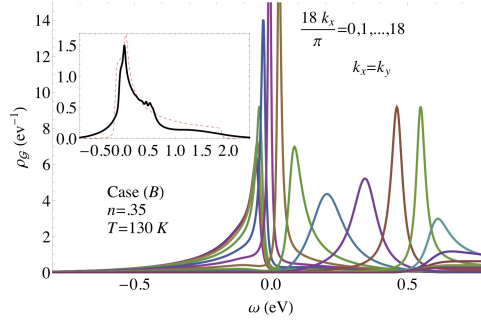


FIG. 15: Case (B) with $(n, T) = (.35, 130K)$. The physical electronic spectral function ρ_G at several k points along the $\langle 11 \rangle$ direction is plotted, showing the evolution of lineshapes across the nodal Fermi surface. At this rather low density, the high frequency tails decay more rapidly than they do at higher densities. The inset shows the ECFL density of states overlaid with the Fermi Gas DOS for the same parameters. The difference between the Fermi Gas and ECFL at this density is much less than was seen in Fig. (14). Note also that the rather sharp QP's at $k \gg k_F$ are visible at this low density, they persist to higher densities as seen below.

to see how the line shapes discussed above in Fig. (16) evolve under the influence of the elastic scattering term. In Fig. (19) low temperature spectral functions are presented with the additional η . The effect of adding a finite η is similar to increasing the temperature, resulting in an increase of the linewidths. However, increasing temperature effects the linewidths more strongly near k_F while η broadens the lineshapes in a more broad and less selective fashion.

H. Optical conductivity

The optical conductivity, $\sigma(\Omega)$, is computed within the bubble approximation here by throwing out vertex corrections:

$$\text{Re}\sigma(\Omega) = \frac{1}{\Omega} \sum_k v_k^2 \int \rho_G(k, \omega) \rho_G(k, \Omega + \omega) (f(\omega) - f(\Omega + \omega)) d\omega \quad (27)$$

The imaginary part of the conductivity can be obtained by a Hilbert transform of the real part. In this purely t - J calculation we must be careful how we combine the real and imaginary parts because the true imaginary part, as opposed to the one computed in the t - J model, will include contributions from the upper Hubbard band and from charge transfer processes which can be appreciable at high frequencies. For our current purposes we will simply discuss QP lifetime effects of two kinds. First we have $1/\tau_\sigma$ which describes a characteristic lifetime which can be extracted from the low frequency curve of $\sigma(\Omega)$. To do so we assume a roughly Lorentzian form and define $1/\tau_\sigma$ by

$$\tau_\sigma \int_0^{1/\tau_\sigma} \sigma(\omega)/\sigma(0) d\omega = \pi/4. \quad (28)$$

This is a momentum averaged quantity. Alternatively we can look at the momentum resolved scattering lifetimes defined as the inverse width of the ARPES lineshape at the Fermi momentum. These scattering rates are displayed in Fig. (20). The ARPES derived $1/\tau$ turns out to be essentially isotropic with differences of $< 1\%$ between nodal and antinodal Fermi surface so only the nodal τ is displayed.

In Case (A) the $1/\tau$ curves taken from ARPES and $\sigma(\omega)$ in Fig. (13) rise quadratically at low temperature in accordance with the standard Fermi liquid picture. We note that the computed conductivity match up on an absolute scale quite well with experimental results in the overdoped regime. For example in Fig. (21) we display the $\text{Re}\sigma(\omega)$ curves for Case (B) along with optical conductivity measurements published by Puchkov et al in²⁵ for an overdoped Thallium compound.

V. CONCLUDING REMARKS

In this work, we have presented a systematic low density expansion results for the t - J model, using the newly developed formalism of *extremely correlated Fermi liquids*, discussed in Ref. (1) and Ref. (5). The expansion in

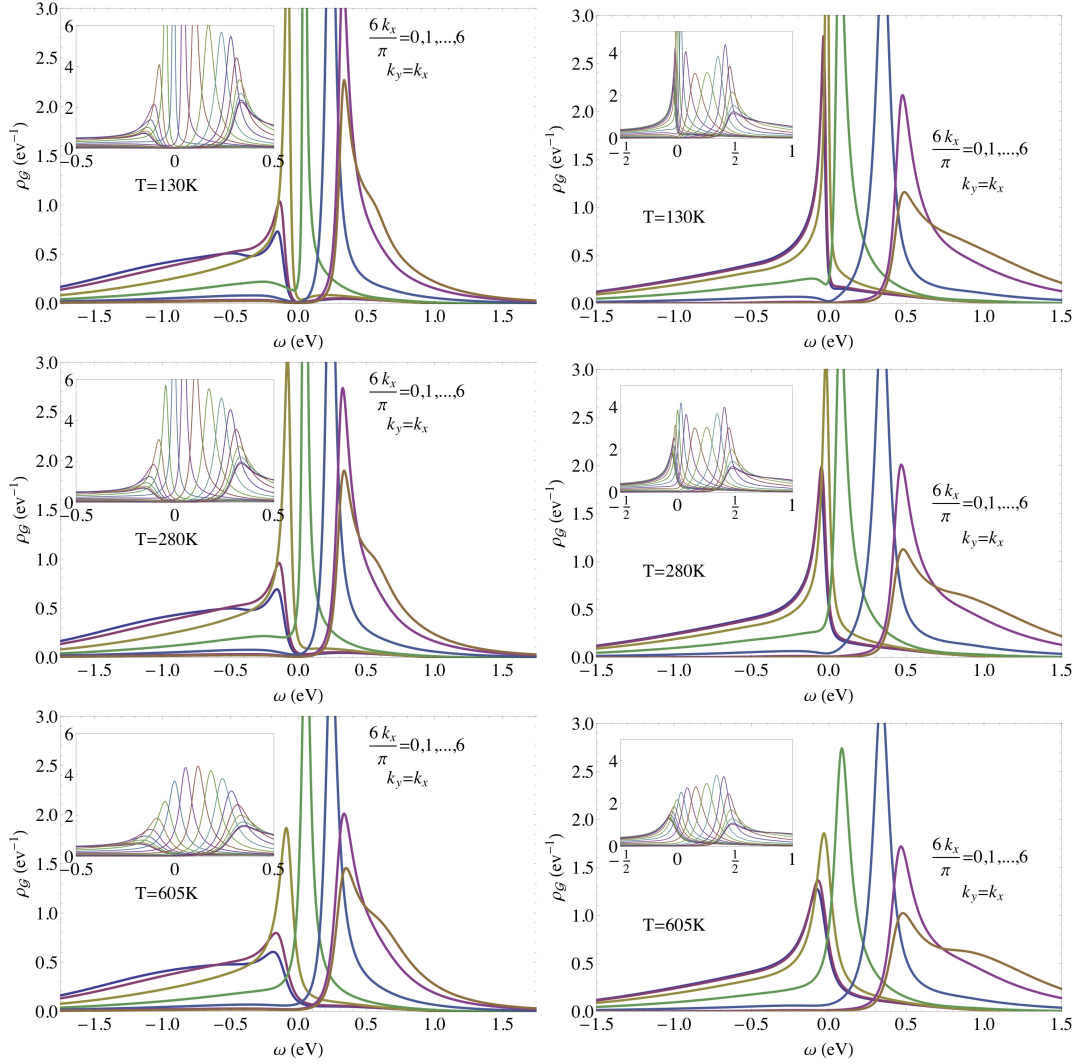


FIG. 16: The physical electronic spectral function ρ_G at several selected k points along the $\langle 11 \rangle$ direction are plotted, showing the evolution of lineshapes across the Fermi surface. Cases (A) and (B) on the left and right respectively with temperature increasing toward the bottom of the panel. The inset in each case zooms out to reveal the height of the lineshapes for all the momenta. While the linewidths near k_F are strongly effected by rising temperature, the incoherent parts particularly at high frequency have very little temperature dependence. Note also that the tails in Case (A) demonstrate an interesting structure near $\omega = -0.4\text{eV}$, a second maximum far from the nominal QP. A similar structure was previously observed in^{2,4}. It appears in Case (A) but not in Case (B). Case (B) displays a local minimum of the linewidths for $k > k_F$, as seen more clearly in Fig. (17).

a parameter λ to second order yields the equations studied here, and has been argued to be the first step in a systematic microscopic study of the t - J model. The range of validity of this calculation is somewhat removed from the most interesting regime of optimal doping, and is self consistently determined to be $n \lesssim 0.7$. This theory differs from the simplified ECFL theory, used to model the optimal doping system line shapes in Ref. (2), in two respects. In the present work the various self energies are calculated self consistently starting from the t - J model rather than postulated- indeed the assumed forms of the self energies turn out to be quite close to the present calculations, thereby validating the approximation. Secondly, the static multiplicative renormalization of the bare band energies ε_k in Eq. (5) is also somewhat different from that in Ref. (2); it is chosen here by a systematic expansion in λ as formulated in Ref. (5). We must therefore be careful in comparing the present results with data at higher particle densities, e.g. closer to optimal doping. A higher order in λ calculation, than the $O(\lambda^2)$ calculation presented here, is needed for addressing higher particle densities. Nevertheless, our work represents the first systematic and essentially analytical calculation of the t - J model at the above mentioned densities, and is interesting for that reason. It is encouraging to note the broad similarity of our results with other numerical works mentioned in the introduction and

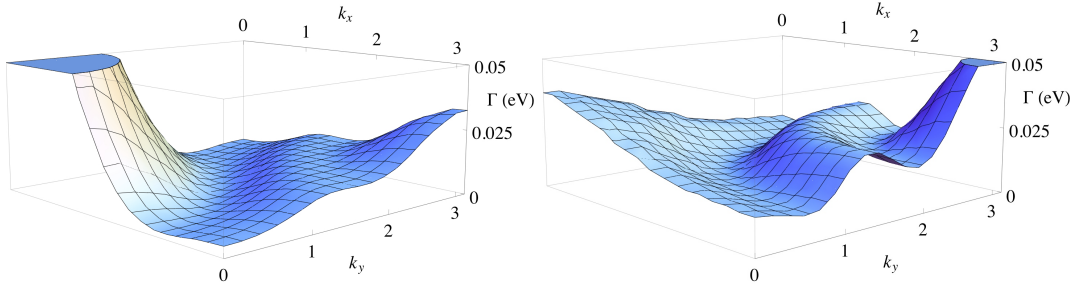


FIG. 17: For Cases (A) and (B) at $(n, T) = (.75, 130K)$ the decay rate calculated from the Dysonian self energy: $\Gamma_k = \rho_\Sigma(k, E_k)$ is plotted in the first quadrant of the Brillouin zone. We see a second set of minima, particularly prominent in Case (B), apart from the expected minimum at the FS. Note also that the value of Γ at the FS is much lower in Case (A) than in Case (B). This occurs because in Case (B) the chemical potential sits near a van Hove singularity resulting in high scattering.

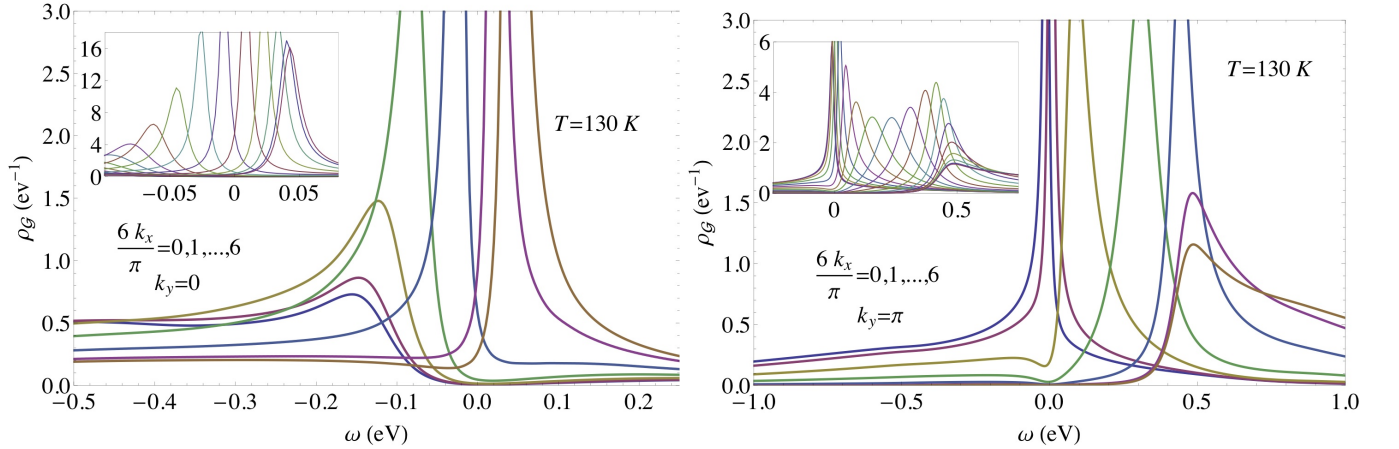


FIG. 18: For $(n, T) = (.75, 130K)$ the spectral function ρ_g is plotted for k 's along the line perpendicular to the anti-nodal FS. For Case (A) on the left and Case (B) on the right this corresponds to the (01) direction and the line from $(0, \pi) \rightarrow (\pi, \pi)$, respectively. The bandwidths seen along these lines are much smaller than those seen along along the nodal line. Thus the momentum dependence of the self energies in the present theory distinguish significantly between the different directions.

text above.

In Section (III) we have presented detailed results for the chemical potential and the momentum distribution function m_k , for two standard sets of band parameters of current interest. We have then detailed the various energy dispersions that emerge in our calculation- these include the bare band dispersion, the MDC dispersion and the EDC dispersion. We also evaluated some measures of the line asymmetry. The so called kink feature is displayed and its dependence on the band parameters is explored. The wave function renormalization Z_k is evaluated at various densities and the Fermi velocity computed along various directions. We observed a second (shadow Fermi) surface, outside the usual Fermi surface, representing a shallow minimum in the quasiparticle relaxation rate. It is different from the usual Fermi surface in location, size and also in the non zero (but small) dissipation at the surface. It is more pronounced for Case (B) than in Case (A), but not very visible in the momentum space distribution function m_k in either case.

The relaxation rates of quasiparticles at finite T and resistivity as well as the local DOS are computed. We displayed the spectral function at various densities and temperatures along different directions in detail. We also explored the effect of elastic impurity scattering on the line shapes in detail. Finally we displayed the optical conductivity and resistivity from this theory, after throwing out vertex corrections, and compared with some data on overdoped systems Ref. (25). As far as possible, all computed objects are presented *on an absolute scale*, using lattice parameters typical of the Cuprate materials, and a fundamental energy scale set by the nearest neighbor hopping $t \sim 3000K$. It is clear that one could tune this scale to better fit a given experiment, e.g. the optical conductivity in Fig. (21) gives a good fit on an absolute scale to Case (A) if we rescale t , whereas it does well in Case (B) with the present scale.

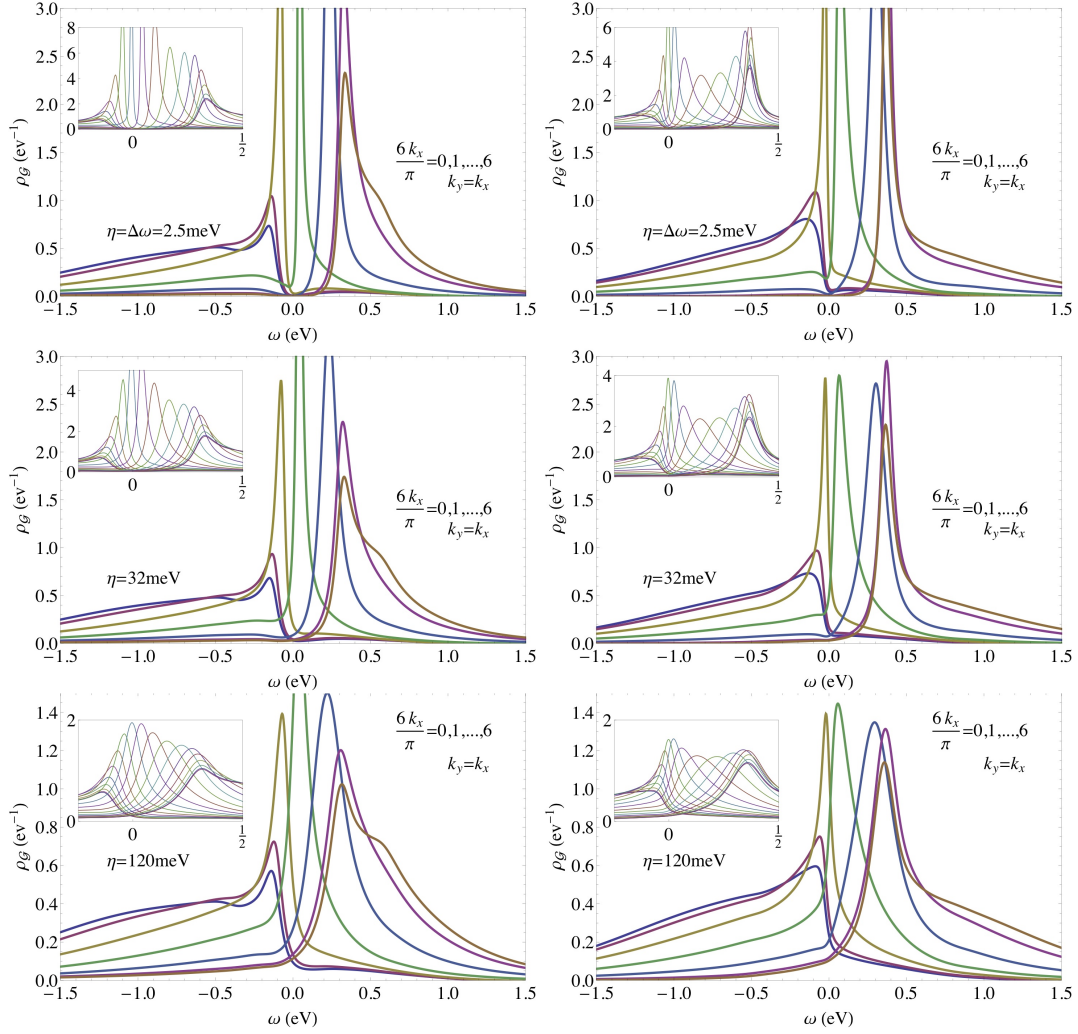


FIG. 19: $(n, T) = (.75, 130K)$ The effect of the elastic scattering term η on the spectral functions ρ_g along $\langle 11 \rangle$ in Cases (A) and (B) (left and right, respectively). For comparison we also include the pristine system with $\eta \sim 0$, and display the resulting curves for three values $\eta = 0, .032, .12$ eV. The two nonzero values are typical for laser and synchrotron ARPES respectively, as argued in Ref. (2). A large (synchrotron ARPES) value of $\eta \sim .12$ eV leads to extended tails and a greatly reduced peak value of the spectra, while the smaller (laser ARPES) value of $\eta \sim .032$ has a less drastic effect on the pristine case.

VI. ACKNOWLEDGEMENTS

This work was supported by DOE under Grant No. FG02-06ER46319. We thank Gey-Hong Gweon for stimulating discussions.

¹ B. S. Shastry, Phys. Rev. Letts., **107**, 056404 (2011)

² G.-H. Gweon, B. S. Shastry, and G. D. Gu., Phys. Rev. Letts., **107** 056404 (2011).

³ B. S. Shastry, Phys. Rev. Letts. **109**, 067004 (2012)

⁴ B. S. Shastry, Phys. Rev. **B 84**, 165112 (2011)

⁵ “Extremely correlated Fermi systems: The Formalism”, B. S. Shastry, arXiv:1207.6826 (2012).

⁶ P. Nozières, *Theory of Interacting Fermi Systems* W. A. Benjamin, Amsterdam, (1964).

⁷ A.A. Abrikosov, L. Gorkov and I. Dzyaloshinski, *Methods of Quantum Field Theory in Statistical Physics*, Prentice-Hall, Englewood Cliffs, NJ (1963)

⁸ G. D. Mahan, *Many-Particle Physics*, Plenum Press, New York (1981)

⁹ W. Stephan, P. Horsch, Phys. Rev. Letts. **66**, 2258 (1991).

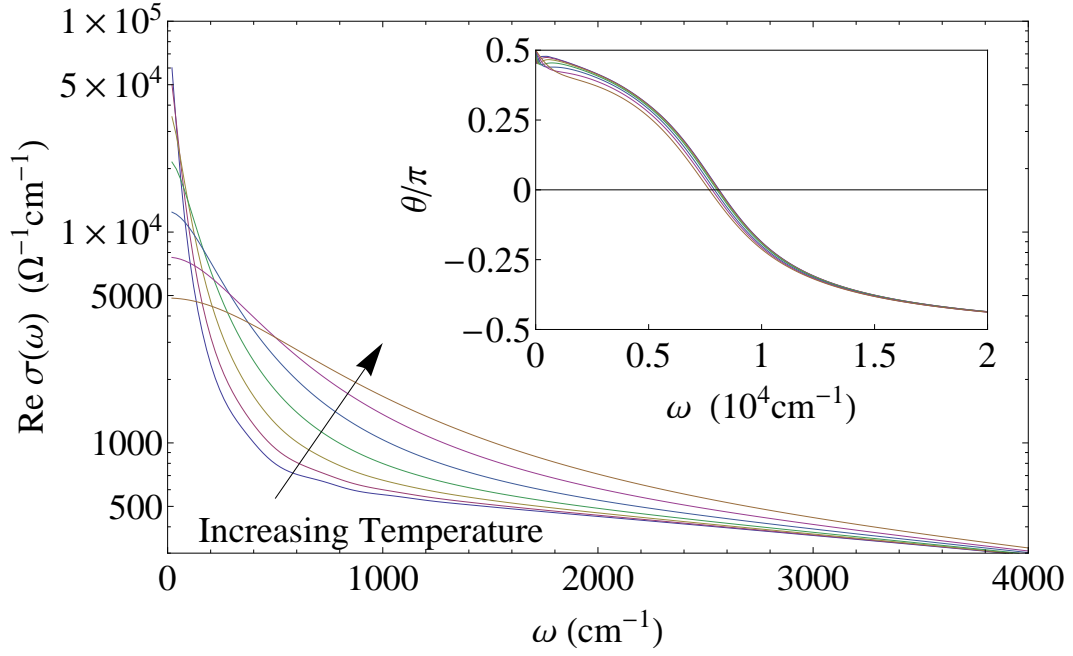


FIG. 20: Case (A) $n = .75$, $T = 60, 90, 130, 190, 280, 410, 605 K$. The optical conductivity is calculated (on an absolute scale) and illustrates how increasing T “fills up” the regime $0 \leq \omega \leq 1000 \text{ cm}^{-1}$ rapidly. The rise of conductivity at very low ω is also inferred from the DC resistivity displayed in Fig. (13). The phase of the complex σ falls off rapidly beyond 4000 cm^{-1} . Results for Case (B) are similar and shown below in Fig. (21).

- ¹⁰ R. R. P. Singh, R. L. Glenister, Phys. Rev. **B 46**, 14313 (1992).
- ¹¹ M. M. Zemljic and P. Prelovsek, Phys. Rev. **B 72**, 075108 (2005).
- ¹² M. M. Zemljic, P. Prelovsek, and T. Tohyama, Phys. Rev. **B 76**, 012502 (2007), M. M. Zemljic, P. Prelovsek, and T. Tohyama, Phys. Rev. Letts. **100**, 036402 (2008).
- ¹³ J. Kokalj and P. Prelovsek, Phys. Rev. **B 75**, 045111 (2007).
- ¹⁴ J. Jaklic and P. Prelovsek, Adv. Phys. **49**, 1 (2000).
- ¹⁵ C. Gros, R. Joynt, T.M. Rice, Phys. Rev. **B 36**, 381 (1986).
- ¹⁶ B. Edegger, V. N. Muthukumar and C. Gros, Adv. Phys. **56** 927 (2007).
- ¹⁷ A. Paramekanti, M. Randeria, and N. Trivedi, Phys. Rev. Letts. **87**, 217002 (2001).
- ¹⁸ B. Moritz, F. Schmitt, W. Meevasana, S. Johnston, E. M. Motoyama, M. Greven, D. H. Lu, C. Kim, R. T. Scalettar, Z.-X. Shen, T. P. Devereaux, New J. Phys. **11**, 093020 (2009).
- ¹⁹ W. Metzner and D. Vollhardt, Phys. Rev. Letts. **62**, 324 (1989).
- ²⁰ A. Georges, G. Kotliar, W. Krauth, and M. J. Rozenberg, Rev. Mod. Phys. **68**, 13 (1996).
- ²¹ X. Deng, J. Mravlje, R. Zitko, M. Ferrero, G. Kotliar, A. Georges, arXiv:1210.1769 (2012).
- ²² W. H. Press, S. A. Teukolsky, W. T. Vetterling, B. P. Flannery, *Numerical Recipes: The Art of Scientific Computing*, Cambridge University Press, New York, NY (1988)
- ²³ T. Valla, A. V. Fedorov, P. D. Johnson, Q. Li, G. D. Gu, N. Koshizuka, Phys. Rev. Letts. **85**, 828 (2000)
- ²⁴ J. Graf, G.-H. Gweon, and A. Lanzara, Physica C: Superconductivity, 460-462, (2007)
- ²⁵ A. V. Puchkov, D. Basov and T. Timusk, J. Phys.: Condens. Matter **8**, 10049 (1996)

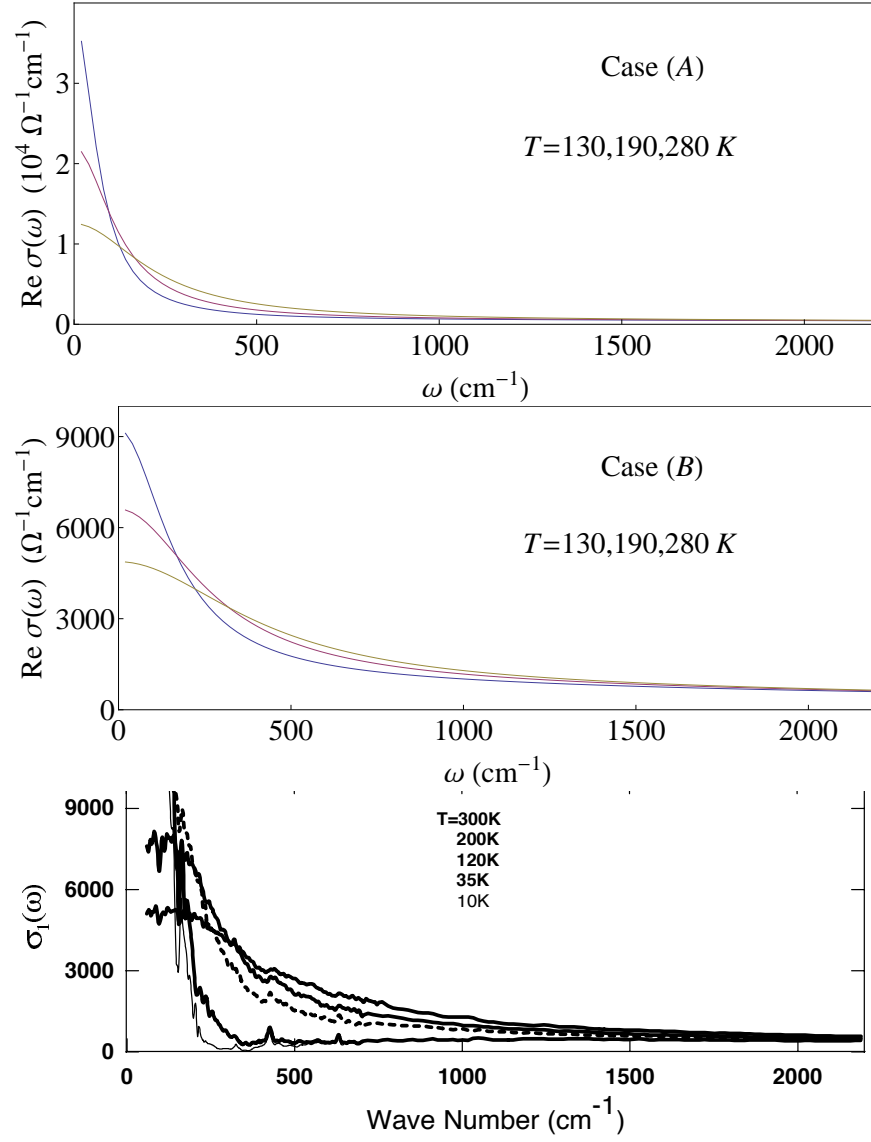


FIG. 21: We make an explicit comparison here with optical conductivity measurement in Puchkov et al in Ref. (25). The experimental data is reproduced from Ref. (25) with the authors kind permission. It pertains to an overdoped Thallium based compound with $T_c = 23\text{ K}$ with a density that is expected to be close to the value assumed in the calculation $n \approx .75$. We note the similarity of magnitude and scale with our Case (B), our Case (A) leads to a bigger value of $\text{Re}\sigma(\omega)$.